Clim Dyn (2012) 38:655–665
DOI 10.1007/s00382-011-1006-4

Reduction of systematic biases in regional climate downscaling through ensemble forcing

Hongwei Yang · Bin Wang · Bin Wang

Received: 11 August 2010 / Accepted: 24 January 2011 / Published online: 23 February 2011

Abstract Simulations of the East Asian summer monsoon for the period of 1979–2001 were carried out using the Weather Research and Forecast (WRF) model forced by three reanalysis datasets (NCEP-R2, ERA-40, and JRA-25). The experiments forced by different reanalysis data exhibited remarkable differences, primarily caused by uncertainties in the lateral boundary (LB) moisture fluxes over the Bay of Bengal and the Philippine Sea. The climatological mean water vapor convergence into the model domain computed from ERA-40 was about 24% higher than that from the NCEP-R2 reanalysis. We demonstrate that using the ensemble mean of NCEP-R2, ERA-40, and JRA-25 as LB forcing considerably reduced the biases in the model simulation. The use of ensemble forcing improved the performance in simulated mean circulation and precipitation, inter-annual variation in seasonal precipitation, and daily precipitation. The model simulated precipitation was superior to that in the reanalysis in both climatology and year-to-year variations, indicating the added value of dynamic downscaling. The results suggest that models having better performance under one set of LB forcing might worsen when another set of reanalysis data is used as LB forcing. Use of ensemble mean LB forcing for assessing regional climate model performance is recommended.

Keywords Uncertainty in regional climate simulation · Ensemble lateral boundary forcing

H. Yang (✉)
LASG, Institute of Atmospheric Physics, Chinese Academy of Sciences, Beijing, China
e-mail: hyang@lasg.iap.ac.cn

B. Wang
Department of Meteorology, University of Hawaii at Manoa, Honolulu, Hawaii

B. Wang
International Pacific Research Center, University of Hawaii at Manoa, Honolulu, Hawaii

B. Wang
LASG, Institute of Atmospheric Physics, Chinese Academy of Sciences, Beijing, China

1 Introduction

Regional modeling is a nonlinear initial-boundary value problem. A nested regional climate model (RCM) simulation is subject to uncertainties originating from lateral boundary (LB) forcing (Miyakoda and Rosati 1977; Anthes et al. 1985; Gustafsson 2002; Mohanty et al. 1990; Jacob and Podzun 1997; Paegle et al. 1997; Denis et al. 2002; Diaconescu et al. 2007). As stated by Giorgi and Bi (2000), initial perturbations dominate simulated biases only in the early stages of a simulation. After the LB information pervades interior of the domain, perturbations in the LB forcing become dominant sources of errors. Although the effect of perturbation in LB forcing shows no clear trend (Wu et al. 2005), the simulated biases induced by LB forcing are generally larger than those induced by initial conditions, even larger than those induced by model resolution and physical parameterizations (Vukicevic and Errico 1990). Biases in the output of a general circulation model can be enlarged by an RCM (Christensen et al. 1997), and missing synoptic information at the LB because of coarse resolution can underestimate seasonal precipitation (Pan et al. 2001). RCM solutions may be particularly susceptible to the choice of LB locations, and positioning the LB in the region of small biases can improve model performance (Qian and Liu 2001; Liang et al. 2001; Xue et al. 2007). In summary, the quality of LB forcing is

vital to RCM simulation. The estimation of the simulation errors arising from LB forcing is a critical element in RCM simulation or downscaling.

Reanalysis data have been popularly used as LB forcing in validation of RCM performance (Christensen et al. 1998; Wang et al. 2003). A number of intercomparison projects of RCM have focused on multi-model simulation with the same reanalysis data as LB forcing (Christensen et al. 1997; Takle et al. 1999; Leung and Ghan 1999; Fu et al. 2005). In the simulation of the 1998 East Asian summer monsoon (EASM), Wang and Yang (2008) found that the Weather Research and Forecast (WRF) model simulations driven by 40-year reanalysis data from the European Centre for Medium-Range Weather Forecasts (ERA-40) and National Center for Environmental Prediction-Department of Energy reanalysis data (NCEP-R2) yield different results. Both have significant deficiencies in reproducing the observed extreme rainfall events. The authors found that the large vapor differences over the Bay of Bengal and the Philippine Sea are the key factors that induce the largely different realizations. The ensemble mean of the two reanalyses is used as driven fields, which lessens the uncertainties in water vapor and other fields, thereby improving the performance of the WRF model simulation.

However, the study of Wang and Yang (2008) was only carried out for the summer of 1998, and only two reanalyses were examined. Their conclusions need to be verified by using long-term simulation and more reanalysis datasets. In particular, the following questions should be addressed: How sensitive is the model solution to different reanalysis forcings? What are the sources of the uncertainties in the large-scale thermal and circulation fields that give rise to the spread of the model solutions? Can we reduce the effects of these uncertainties to improve the performance of the WRF model?

To answer these questions, we are motivated to simulate the EASM from 1979 to 2001, a total of 23 summers, driven by NCEP-R2, ERA-40, the Japanese 25-year reanalysis (JRA-25), and their ensemble mean. The model description is provided in Sect. 2, and the experimental design is described in Sect. 3. Section 4 presents our analysis of the errors in the experiments driven by the individual reanalysis. The sources of the simulated errors are discussed in Sect. 5. In Sect. 6, we evaluate the experiment driven by the ensemble mean of the reanalyses. The added value of the dynamic downscaling is discussed in Sect. 7. The final section presents the summary and discussion.

2 Model and data

The WRF model (Skamarock et al. 2005), a primitive equation model using sigma coordinates, is used in this study. The physical processes used include Betts-Miller-Janjic cumulus parameterization (Janjic 2000), rapid radiative transfer model for long-wave radiation (Mlawer et al. 1997), Dudhia (1989) scheme for shortwave radiation, Lin cloud microphysics (Lin et al. 1983; Chen and Sun 2002), Noah's land surface model (Chen and Dudhia 2001), and Yongsei University planetary boundary layer scheme (Noh et al. 2003).

The forcing fields are air temperature, specific humidity, horizontal winds, and geopotential height at pressure levels, which are interpolated by a preprocessor to match the resolution of the WRF model. In addition, the initial conditions include surface pressure, sea-level pressure, temperature and moisture at a 2-m height, horizontal winds at a 10-m height, skin temperature, soil moisture, and soil temperature. The skin temperature over the ocean is considered sea surface temperature.

Three reanalysis datasets were used as sources of LB forcing: NCEP-R2 (Kanamitsu et al. 2002), ERA-40 (Uppala et al. 2005), and JRA-25 (Onogi et al. 2007). They are relaxed in a buffer zone of 10 grid boxes, where the influence of the reanalyses data decreases from the boundary to the center of the model domain. The land surface model uses the following datasets: 30-s topographic data, U.S. Geological Survey land-use data, and 5-min soil-type data from the Food and Agriculture Organization of the United Nations.

The ensemble mean of the NCEP-R2, ERA-40, and JRA-25 was defined as the "perfect" data to validate the simulated circulation. Two datasets were used to verify the simulated precipitation—the satellite-based Global Precipitation Climatology Project (GPCP) monthly precipitation with a resolution of 2.5° × 2.5° (Adler et al. 2003) and the gauge-based Monsoon Asia Analysis precipitation (with a resolution of 0.5° × 0.5°, constructed by the Asian Precipitation—Highly—Resolved Observational Data Integration Towards Evaluation [APHRODITE] of the Water Resources project; Yatagai et al. 2009). For comparison with model results, both GPCP and gauge precipitation were interpolated into the grids of the model using bilinear interpolation. The validation of bilinear interpolation was verified by comparison of four-year (1998–2001) climatological June–July–August (JJA) mean rainfall between Tropical Rainforest Measuring Mission (TRMM) 3B43 (Adler et al. 2000) and GPCP at 0.5° and 2.5° resolutions. The TRMM 3B43 is derived from microwave and infrared satellite measurements and surface rain-gauge observations, and is available as a monthly mean product at 0.25° resolution. To validate the simulated precipitation over the entire model domain at the same time, the blended data of the rain gauge over land and the GPCP over sea were used (i.e., the oceanic grid points of the bilinear interpolated rain gauge data were filled with the bilinear interpolated GPCP data).

3 Experimental design

In this study, the simulation period is comprised of the 23 rainy seasons in East Asia from 1979 to 2001. In each year, the WRF model ran from 00Z 22 April through 18Z 31 August. The 9 days before 1 May were considered as "spin-up" period (Giorgi and Mearns 1999). The spin-up time of 9 days may be insufficient for adjusting the atmosphere to land surface anomalies. Fortunately, the soil moisture-precipitation feedback is much less important than the moisture flux convergence anomaly during the Asian monsoon season (Douville et al. 2001). Our results confirmed that evaporation is relatively stable and that the change in precipitation is highly consistent with the change in moisture flux convergence (figure not shown). The output from 1 May to 31 August was analyzed.

The model domain covers the EASM region centered at 25°N and 115°E, from 5° to 45°N and from 90° to 140°E. The grids of the model consist of 101 (zonal) × 92 (meridional) horizontal grid points at about a 50-km grid space and 31 vertical layers up to 50 hPa. Figure 1 shows the domain and topography map. The steep slope of the Tibetan Plateau is located west of the domain. The Bay of Bengal, a source of abundant moisture, is located southwest of the domain. The western North Pacific (WNP) subtropical high, which dominates the evolution of seasonal monsoon precipitation, is located east of the domain.

To study the effect of the LB conditions on the WRF model, we initially designed three sensitivity experiments, in which the NCEP-R2, ERA-40, and JRA-25 reanalyses were used as initial and LB conditions. The experiments were labeled Exp-R2, Exp-40, and Exp-25, respectively. Because Wang and Yang (2008) indicated the ensemble mean of the NCEP-R2 and ERA-40 in their study yields the best result, in this study we designed another experiment driven by the ensemble mean of the three reanalyses and referred to it as the control experiment (CTL). Generally, the reanalyses datasets are available at 6-h intervals with a horizontal resolution of 2.5° × 2.5° on identical grids. As the NCEP-R2 and ERA-40 have only 17 pressure levels, the same pressure levels of the JRA-25 were selected from its original 23. The JRA-25 only has moisture at 12 pressure levels up to 100 hPa that are identical to the 12 lower levels of the other reanalyses. The moisture of the JRA25 at the 5 upper levels was filled with zero. Thus, the three reanalyses were prepared on the same grid and were used to generate the LB conditions for the four experiments. Different from the ERA-40 and JRA-25, the surface data of NCEP-R2 is 1.85° × 1.85° and was interpolated to 2.5° × 2.5° grid with a bilinear scheme. The initial conditions of experiments Exp-R2, Exp-40, and Exp-25 were taken from the NCEP-R2, ERA-40, and JRA-25 reanalyses, respectively. The initial conditions of the CTL were created from the mean values of the three reanalyses. The physical parameterizations and model configuration are uniform for all experiments. All model parameters are taken with the default values without tuning.

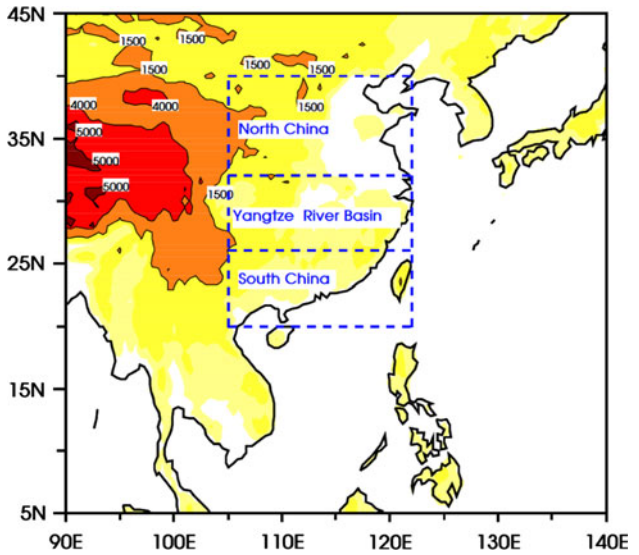

Fig. 1 Simulation domain and topography (color shading in units of meters). Topographic contours of 1,500, 4,000, and 5,000 m are highlighted. Analysis areas over land enclosed by dashed lines refer to South China (20°–26°N, 105°–122°E), the Yangtze River Basin (26°–32°N, 105°–122°E), and North China (32°–40°N, 105°–122°E)

4 Systematic biases in simulations forced by individual reanalysis

Forced by different LB conditions, the three sensitivity experiments yielded different systematic biases in their simulations of JJA mean low-level circulations. Figure 2b, c, and d show the biases in the 850-hPa circulations produced by Exp-R2, Exp-40, and Exp-25, respectively. The biases were defined by the deviation of the RCM simulations from the ensemble mean of NCEP-R2, ERA-40, and JRA-25. The bias in Exp-R2 (Fig. 2b) was a notable anticyclonic high-pressure bias over eastern China and the surrounding ocean. The bias in Exp-40 (Fig. 2c) was larger than that in Exp-R2 but it had an opposite sign: a major cyclonic low-pressure bias was located over eastern China and the East China seaboard centered in Taiwan. The bias in Exp-25 (Fig. 2d) was a high-pressure bias observed mainly over WNP and the Indochina Peninsula and its associated circulations. These different biases reflected the large uncertainty in experiments driven by individual reanalysis. The WNP subtropical high is the key weather system of the EASM. Therefore, the discrepancies have marked effects on the summer monsoon precipitation and circulation in the experiments.

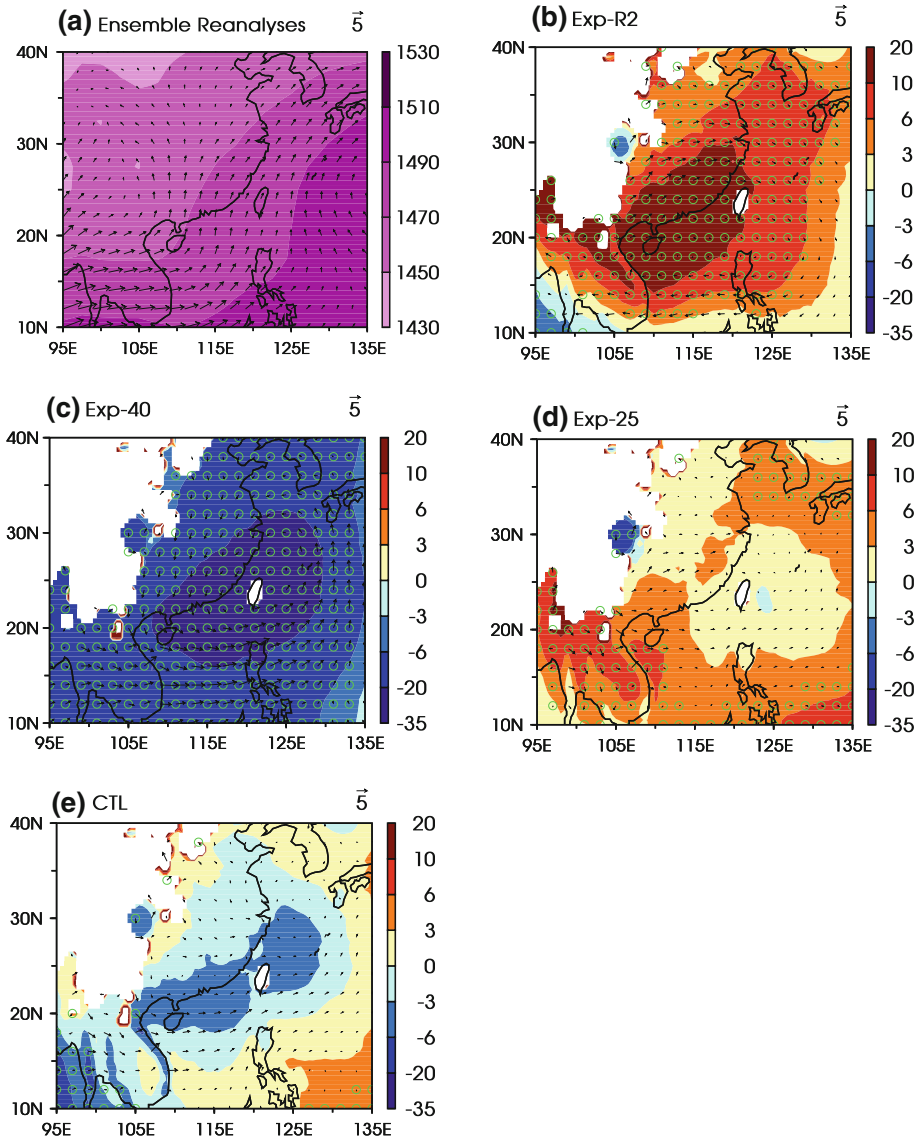

Fig. 2 **a** The climatological June–July–August (JJA) mean geopotential height (shading in units of meter) and horizontal winds (vector in units of m s^{-1}) at 850 hPa that are derived from the ensemble mean of NCEP-R2, ERA-40, and JRA-25 reanalyses data. Respectively, **b**, **c**, **d**, and **e** are the biases simulated with lateral boundary (LB) conditions derived from **b** the NCEP/DOE reanalysis 2 (NCEP-R2), **c** the ECMWF 40-year reanalysis (ERA-40), **d** the Japanese 25-year reanalysis (JRA-25), and **e** ensemble mean of the three reanalyses. All the biases are defined by the deviation of RCM simulations from the ensemble mean of NCEP-R2, ERA-40, and JRA-25. The *green circles* indicate the significant areas with 95% confidence level in the difference of geopotential height by t test

The biases in the low-level circulations were also observed in individual years. Figure 3 shows the root mean square error (RMSE) of the simulated JJA mean geopotential height at 850 hPa, relative to the ensemble mean (of NCEP-R2, ERA-40, and JRA-25) in each of the 23 years. Only the sensitivity experiments are considered here (i.e., only the red, green, and blue points in Fig. 3). Of the three sensitivity experiments, Exp-25 yielded the geopotential height most similar to the ensemble mean of three reanalyses, i.e., Exp-25 had the smallest RMSE in 17 out of 23 years. Exp-R2 produced results that were, to a large extent, closer to the ensemble mean than those of Exp-40 in most years. The variations in model performance provided evidence that the systematic differences in large-scale forcing could systematically influence the RCM in an identical manner in most years, but not in all years. Therefore, reducing the systematic biases of large-scale forcing may generally improve RCM performance.

The different simulated results were observed not only in dynamic fields but also in seasonal and daily mean precipitation. The performance of the model in terms of seasonal rainfall is shown in Fig. 4, which presents the spatial correlation coefficients between the simulation and the rain-gauge observation of the 23 JJA mean rainfall in three regions over land (i.e., North China, the Yangtze River Basin, and South China). Among the three sensitivity experiments, Exp-R2 had the highest mean correlation coefficient (i.e., 0.45) of the 69 JJA correlations (23 years among the three regions). The corresponding correlation coefficient means of Exp-25 and Exp-40 were 0.33 and 0.22, respectively. Figure 5 shows the daily precipitation averaged over North China, the Yangtze River Basin, and South China. Measured by the correlation coefficient and RMSE relative to the observation, Exp-40 performed best in the Yangtze River Basin, whereas Exp-25 performed best in North China and South China.

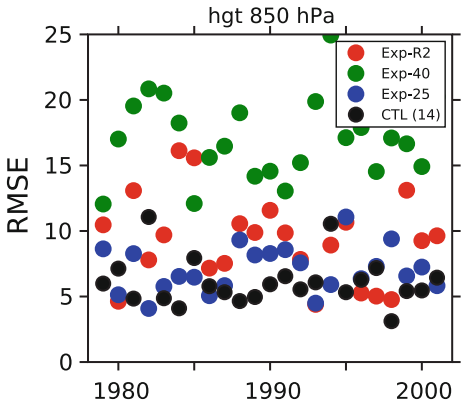

Fig. 3 RMSE of the simulated JJA mean geopotential height at 850 hPa relative to the ensemble mean of NCER-R2, ERA-40, and JRA-25 in 23 years. The *red*, *green*, *blue*, and *black dots* denote RMSE of Exp-R2, Exp-40, Exp-25, and CTL, respectively. The *bracketed number* in the legend is the total number of years in which the CTL experiment has the smallest RMSE

The climatological summer precipitation of the three sensitivity experiments also exhibited distinctive features. Relative to the observed climatological summer precipitation, which is the blended data of the rain gauge over land and the GPCP over sea, the pattern correlation coefficients of the simulated climatological summer precipitation of Exp-R2, Exp-40, and Exp-25 were 0.71, 0.74, and 0.67, respectively (Table 1). Exp-R2 notably underestimated precipitation over the Philippine Sea, Korea, and Japan. Exp-40 overestimated precipitation over almost all of the ocean areas and underestimated precipitation over land. Exp-25 produced more precipitation than was observed mainly over the Philippine Sea (figures not shown).

In addition to the climatological summer precipitation, the inter-annual variations in seasonal precipitation of the three sensitivity experiments, as represented by the temporal standard deviation of the seasonal precipitation, also differed remarkably. Relative to the inter-annual variation in seasonal precipitation of the blended observation, the pattern correlation coefficients of the corresponding fields of Exp-R2, Exp-40, and Exp-25 were 0.53, 0.61, and 0.61, respectively (Table 1). Compared with the blended observation, seasonal precipitation in Exp-R2 showed notably more inter-annual variations over the Bay of Bengal and the Indo-China Peninsula. In addition to the same features in Exp-R2, seasonal precipitation in Exp-40 and Exp-25 showed larger inter-annual variations than the blended observation over the South China Sea and the Philippine Sea (figures not shown).

With the same configuration, the aforementioned differences among the three sensitivity experiments could only have been caused by the different LB forcings. Thus far, however, the component of LB forcing that causes

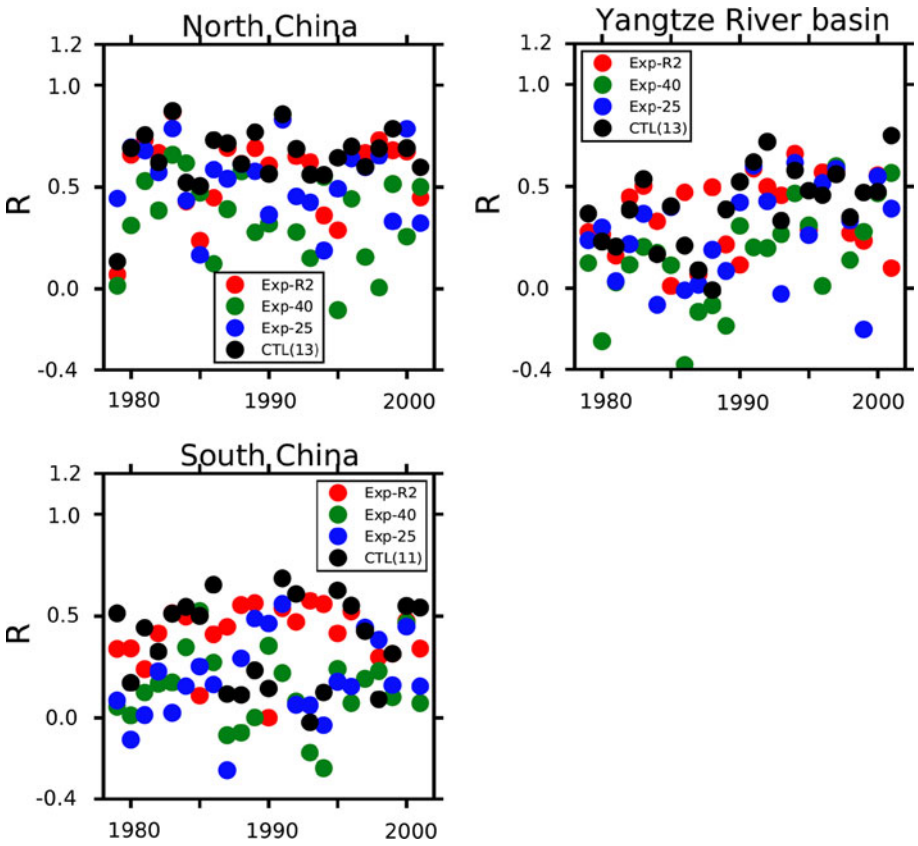

Fig. 4 Spatial correlation coefficients (R) of the simulated JJA precipitation relative to the observed gauge rainfall in 23 years over the land areas of North China, the Yangtze River basin, and South China (see Fig. 1 for definition). The *red*, *green*, *blue*, and *black dots* denote R of Exp-R2, Exp-40, Exp-25, and CTL, respectively. The *bracketed number* in the legend is the total number of years in which the CTL experiment has the largest R

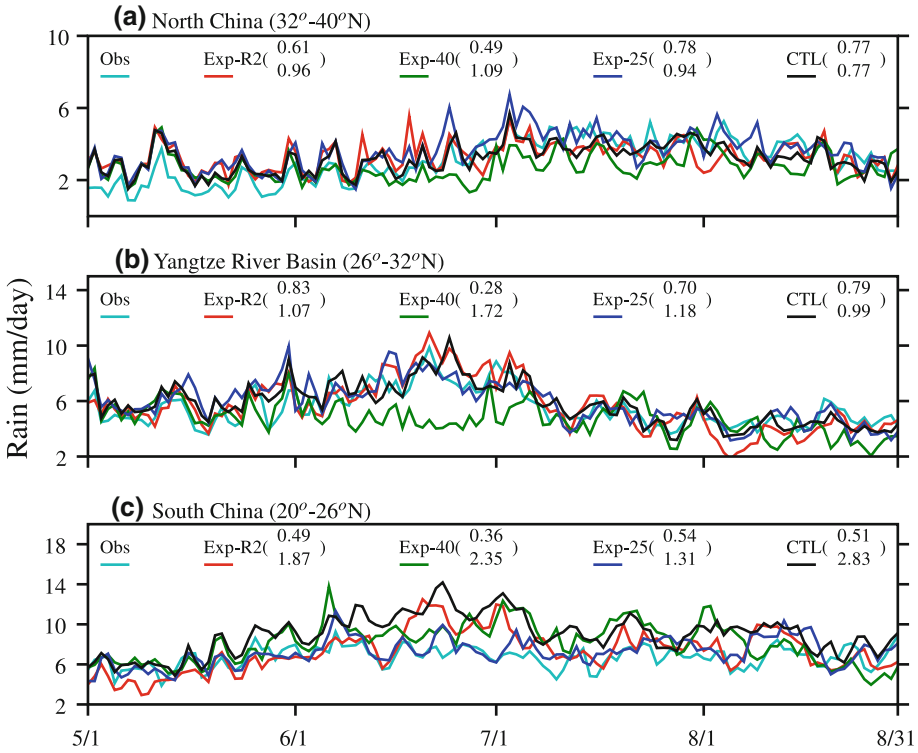

Fig. 5 Climatological daily precipitation rates (mm day^{-1}) from May 1 to August 31, averaged over the land area of **a** North China, **b** the Yangtze River Basin, and **c** South China (see Fig. 1 for definition). The *cyan*, *red*, *green*, *blue*, and *black lines* denote the rain gauge observation, Exp-R2, Exp-40, Exp-25, and CTL, respectively. Correlation coefficients between observed and simulated curves are the *upper numbers* in the brackets in the legend; root mean square errors between observed and simulated curves are the *lower numbers* in the brackets in the legend

Table 1 Spatial correlation coefficients (R) of climatological mean (CM) and inter-annual variation (IAV) of seasonal precipitation over model interior domain (10°–40°N, 95°–135°N) between the blended observation and reanalyses (experimental results) of NCEP-R2 (Exp-R2), ERA-40 (Exp-40), JRA-25 (Exp-25), and ensemble mean of reanalyses (CTL)

R	NCEP-R2 (Exp-R2)	ERA-40 (Exp-40)	JRA-25 (Exp-25)	Ensemble (CTL)
CM	0.52 (0.71)	0.61 (0.74)	0.58 (0.67)	0.65 (0.80)
IAV	0.35 (0.53)	0.43 (0.61)	0.44 (0.61)	0.56 (0.64)

these large differences, as well as its mechanism, remains unknown. A detailed discussion of these issues is presented in the next section.

5 The source of the systematic biases

To clarify which field in LB forcing had the largest difference among the three reanalyses, we investigated the LB forcing variables: horizontal wind, geopotential height, absolute humidity, and temperature. We used the spatial average of noise-to-signal ratio (NSR; the spatial average of the inverse of signal-to-noise ratio), on each side of the LBs to determine the relative differences of a variable among the three reanalyses. For example of temperature at the western boundary, we first calculated the climatological JJA mean temperature for the three reanalyses. Then for each point on the western boundary, we calculated the noise-to-signal ratio from the three climatological JJA mean temperatures. Finally, the NSR was defined as the spatial average of the noise-to-signal ratio at the western boundary. Larger (smaller) values of NSR mean that the relative differences of a variable among the three reanalyses were larger (smaller). Near a wind shear, the u or v component of the horizontal wind becomes very small, leading to a huge NSR value that cannot reflect the actual differences in winds among the three reanalyses. Therefore, wind speed was used to measure the wind differences instead of u or v.

Table 2 shows that the NSRs of absolute humidity had the largest values on each side of the lateral boundaries, which means that the difference in absolute humidity among the three reanalyses is the largest among the four variables. The NSRs of wind speed were less than half those of absolute humidity. The very small NSRs of geopotential height and temperature indicated that almost no relative differences in these fields existed.

The large relative differences in absolute humidity at the eastern, western, and southern boundaries were most likely the key factors producing the large differences in the sensitivity experiments. Although the NSR value (0.18) was largest at the northern boundary, the spatial average of the

Table 2 Spatial average of noise-signal ratio (NSR) of large-scale forcing fields at the western, eastern, southern, and northern lateral boundaries. The symbols WS, z, a, and T represent wind speed, geopotential height, absolute humidity, and air temperature, respectively. The spatial average of the signal (mean) of absolute humidity is also shown

NSR/mean	WS	z	a	T
West	0.06	0.00	0.16/5.49	0.00
East	0.03	0.00	0.13/6.14	0.00
South	0.05	0.01	0.11/6.65	0.00
North	0.03	0.00	0.18/2.85	0.00

mean absolute humidity (i.e., an approximation of the signal in NSR) was the smallest (i.e., 2.85), indicating that the relative difference was actually minimal.

The JJA mean vertical profiles of moisture flux across the western, southern, and eastern lateral boundaries below 300 hPa are presented in Fig. 6. In conjunction with Fig. 6, the zonal and meridional features of moisture uncertainty are shown in Fig. 7, for which the JJA mean vertically integrated moisture fluxes from the surface to 300 hPa across the three lateral boundaries were calculated. The moisture flux across the northern boundary is not shown because it is negligible. Fluxes are positive towards the north and east.

The three major channels that supply abundant moisture into the EASM and affect its variability are the strong low-level jet over the Bay of Bengal, the cross-equatorial Southern Hemisphere flows, and the circulation over the WNP (e.g., Ding and Sikka 2006; Zhou and Yu 2005). To investigate the roles of these moisture channels, we divided the western and eastern boundaries into two parts at 26°N. At the western boundary, the large differences in moisture flux were concentrated below 700 hPa (Fig. 6a) over the Bay of Bengal (Fig. 7). ERA-40 reanalysis exhibited the largest moisture flux, whereas JRA-25 reanalysis showed the smallest in this area. At the southern boundary, large differences in moisture flux appeared at middle levels and within the boundary layer (Fig. 6b). ERA-40 reanalysis showed the largest flux in this area (Fig. 7). The flux in NCEP-R2 was smaller than that in JRA-25 at the middle levels and was larger at the low-level and within the boundary layer in this area (Fig. 6b). Different from the western and southern boundaries, the positive moisture fluxes above 900 hPa at the eastern boundary were outflows of water vapor, whereas the negative moisture fluxes

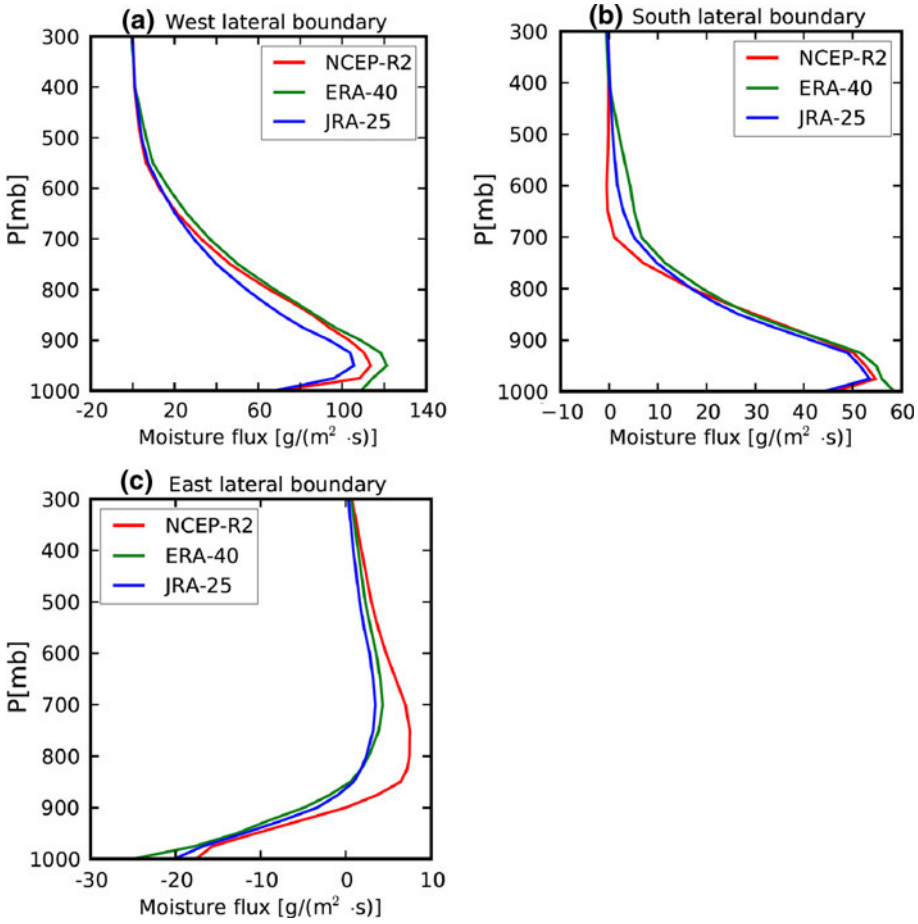

Fig. 6 Climatological JJA mean vertical profiles of moisture fluxes from the surface up to 300 hPa, averaged along the **a** western, **b** southern, and **c** eastern lateral boundaries. The *red*, *green*, and *blue lines* indicate results obtained from NCEP-R2, ERA-40, and JRA-25 reanalyses

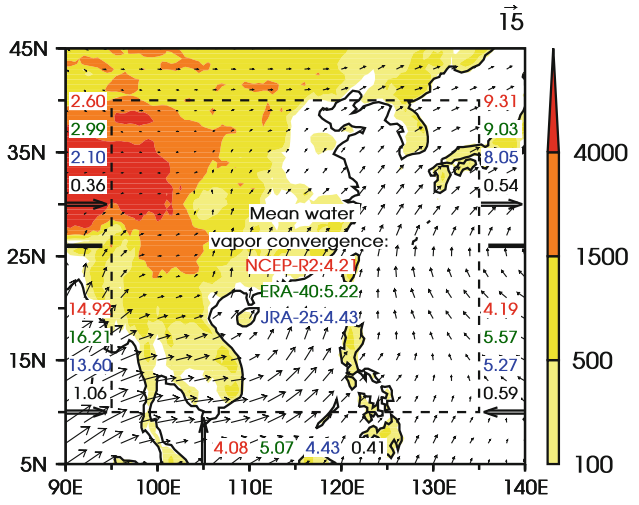

Fig. 7 Climatological summer (JJA) mean of total vertical integrated water vapor fluxes (*colored numbers* in units of g m^{-2} s^{-1}) through the various segments of the lateral boundaries. The *colored numbers* in the center of the domain indicate the JJA mean domain averaged total water vapor convergence per unit area of the large-scale forcing (in units of mm day^{-1}). The values marked in *red*, *green*, and *blue* are derived from NCEP-R2, ERA-40, and JRA-25 respectively, whereas the numbers in black are the standard deviations of the colored numbers in the same column or row. The *thick arrows* indicate the direction of water vapor transport. The *arrows* in the model domain represent the climatological JJA mean total vertical integrated water vapor transport vectors derived from the ensemble mean of NCEP-R2, ERA-40, and JRA-25 with a unit of 15 g m^{-2} s^{-1}. Topography is shaded according to units of meters. The *dashed box* indicates the interior domain. The area between the lateral boundaries and *dashed box* indicates the buffer zone

in the boundary layer were influxes (Fig. 6c). Among the three reanalyses, the amount of moisture in NCEP-R2 reanalysis going out of the domain is the largest at levels above 900 hPa (Fig. 6c) as well as on the northern flank of the WNP subtropical ridge located at 26°N (Fig. 7). In the boundary layer to the southern flank of the WNP subtropical ridge, NCEP-R2 reanalysis transferred the smallest amount of moisture into the domain (Figs. 6c, 7).

To determine the roles and uncertainties of the moisture flux channels, we used the mean moisture fluxes and their standard deviations to measure the uncertainties of the moisture flux. The largest mean value of 14.92 g m^{-2} s^{-1} and the largest standard deviation of 1.06 g m^{-2} s^{-1} occurred in the southern part of the western boundary over the Bay of Bengal (Fig. 7), indicating that the Bay of Bengal was not only the largest moisture source but was also the location where moisture flux introduced the greatest uncertainty. The second-largest standard deviation of 0.59 g m^{-2} s^{-1} was seen over the Philippine Sea from 5° to 26°N, but the second-largest mean fluxes occurred over the northern flank of the WNP subtropical ridge (Fig. 7). The three reanalyses held relatively less moisture transport over the Philippine Sea; the uncertainty there was large. The huge discrepancies in the moisture transport over the Bay of Bengal and the WNP among the three reanalyses were mainly caused by a shortage of observations over these oceanic areas, which agrees with the findings of Wang and Yang (2008).

The climatological JJA mean moisture flux convergences from the three LBs are shown at the center of Fig. 7. The convergence in the ERA-40 reanalysis (5.22 mm day^{-1} m^{-2}) was about 24% higher than that in the NCEP-R2 reanalysis (4.21 mm day^{-1} m^{-2}). The moisture uncertainties went through the buffer zone and eventually influenced the hydrological cycle of the model in the interior domain.

6 Improved simulation using ensemble mean LB forcing

The different reanalysis data were produced using models with different parameterizations of physical processes. The errors in the physical parameterizations of the models may be considered independent of each other; thus, the errors in different reanalysis datasets may be considered random. If so, an ensemble mean of these reanalyses would potentially reduce the random errors present in individual reanalysis datasets. A similar rationale was employed in the multi-model ensemble (MME) climate prediction (e.g., Krishnamurti et al. 1999), in which the MME prediction outperforms that of any single-model component (e.g., Palmer et al. 2000; Shukla et al. 2000; Wang et al. 2004).

The climatology and inter-annual variability of the ensemble mean precipitation derived from the three reanalysis datasets matched the blended observational counterparts better than any individual reanalysis did (Table 1). This provides evidence that ensemble reanalysis datasets indeed reduce errors in the precipitation field.

In this work, the ensemble means of winds, geopotential height, temperature, and humidity from the NCEP-R2, ERA-40, and JRA-25 reanalyses were used as LB forcing in the CTL. The physical parameterizations and model configuration in the CTL are identical to those in the sensitivity experiments.

Ensemble forcing improved the simulated precipitation. Figure 4 shows that the CTL outperformed the three sensitivity experiments in terms of spatial patterns of seasonal precipitation in all three land regions (North China, the Yangtze River Basin, and South China). In 23 years, the CTL produced the best seasonal precipitation in 13 years in North China, 13 years in the Yangtze River Basin, and 11 years in South China. The CTL exceeded the runner-up (Exp-R2) in 7 years in North China, 5 years in the Yangtze River basin, and 3 years in South China. In three regions and 23 years, the CTL run achieved the highest score of a

mean correlation coefficient of 0.48. Figure 5 shows the daily precipitation averaged over North China, the Yangtze River Basin, and South China. Although the CTL run did not achieve the highest score in correlation coefficients, it was comparable to the best sensitivity experiment in all the regions. Thus, the overall performance of the CTL run (0.69), denoted by the averaged correlation coefficients among three regions, exceeded those of Exp-R2 (0.64), Exp-40 (0.38), and Exp-25 (0.67). The RMSEs in Fig. 5 show that the CTL achieved the highest score over both North China and the Yangtze River Basin, whereas the CTL simulated too much precipitation in June and obtained the lowest score in South China. Table 1 provides the pattern correlation coefficients of climatological mean and inter-annual variation in summer precipitation between the simulation and observation. The CTL achieved the best correlation score for the climatological mean (0.80) and for inter-annual variations (0.64).

The superiority of the CTL was also observed in low-level circulation. Figure 2e shows model biases of 850-hPa geopotential height and horizontal winds of the climatological JJA mean in the CTL. Compared with Exp-R2 and Exp-40 in Fig. 2b and c, the CTL dramatically reduced circulation biases, only slightly underestimating the geopotential height over the central domain and overestimating the geopotential height near the southern and eastern boundaries. Compared with Exp-25, the CTL also produced smaller biases over WNP, Indochina Peninsula, and the northeastern area of the domain. The significant biases of the CTL (Fig. 2e, green circles) existed only at the Bay of Bengal and the southern Philippine Sea. The cyclonic wind biases over the domain center in the CTL were insignificant.

The superiority of the CTL was also observed in seasonal mean circulation in each individual year. The black dots in Fig. 3 represent the RMSE of the CTL relative to the ensemble of the reanalyses. In 23 years, the CTL run presented the smallest RMSE in 14 years and only tended to have larger RMSE in 1982 and 1994, compared with Exp-R2 and Exp-25. The results in this study suggest that the use of ensemble forcing systematically reduced the biases in RCM simulations in most of the years, but not in all years.

The results shown in Figs. 2 and 5 and Table 1 indicate that, with the ensemble mean LB condition, the WRF model produced smaller biases in summer mean circulation and precipitation, inter-annual variation in seasonal precipitation, as well as in most cases of daily precipitation than those simulated using individual reanalysis forcing. In terms of the number of summers in which the model produced the smallest biases in seasonal mean, the CTL run also outperformed all sensitivity experiments in both seasonal circulation and precipitation (Figs. 3, 4).

7 The added value of RCM downscaling

This section analyzes the added values of RCM simulations against their corresponding large-scale forcings, which is different from the value of ensemble approach. Against the blended observation, the pattern correlations of the simulated climatological mean summer precipitation in Exp-R2, Exp-40, Exp-25, and CTL were 0.71, 0.74, 0.67, and 0.80, respectively. The values were higher than those of the corresponding reanalysis values of 0.52, 0.61, 0.58, and 0.65 (Table 1). The pattern correlations of the inter-annual variability in summer precipitation between simulations and observation in Exp-R2, Exp-40, Exp-25, and CTL were 0.53, 0.61, 0.61, and 0.64 respectively, whereas the correlations between reanalyses and observation in NCEP-R2, ERA-40, JRA-25, and their ensemble were 0.35, 0.43, 0.44, and 0.56, respectively.

These results show that both sensitivity and CTL experiments exhibited appreciably higher performance for climatological mean and inter-annual variability in summer precipitation than those in the corresponding reanalyses, although the precipitations of the reanalyses are quite close to the observation due to assimilation. This added value shows that the WRF model produced the expected small-scale information, and therefore, had value-added dynamic downscaling skills on the EASM.

8 Summary

Simulations for 23 years (1979–2001) of the East Asian summer monsoon (EASM) were carried out using the WRF model forced by three reanalysis datasets (i.e., NCEP-R2, ERA-40, and JRA-25) and their ensemble mean (algebraic average of the three reanalyses). The simulation results using three different reanalysis forcings showed large discrepancies in mean circulation and precipitation, inter-annual variations in seasonal precipitation, and daily precipitation (Table 1; Figs. 2, 3, 4, 5). Diagnostic analysis reveals that the differences in the large-scale moisture forcing fields at the eastern, western, and southern boundaries were responsible for the large discrepancies. Surprisingly, the climatological mean water vapor convergence into the model domain computed from ERA-40 was about 24% higher than that computed from the NCEP-R2 reanalysis. The largest moisture uncertainty was found over the Bay of Bengal, and the second-largest moisture uncertainty appeared over the Philippine Sea.

As expected, the experiment forced by the ensemble LB condition (CTL) reduced the simulation biases in climatological summer circulation and precipitation, inter-annual variation in seasonal precipitation, and in most cases of daily precipitation in the East Asian region. In terms of the

number of summers in which the model produced the smallest biases in seasonal mean, the CTL outperformed all sensitivity experiments in both seasonal circulation and precipitation. This result indicates that the biases in RCM simulation may be reduced using an "ensemble" average of three or more reanalyses as LB forcing, which agrees with the results obtained by Wang and Yang (2008) for a specific summer.

The premise of using ensemble reanalyses as driving fields is the consideration that the errors in different reanalyses are independent of each other, and an ensemble mean would potentially reduce the uncertainties by canceling out random errors. Evidence supporting this hypothesis is that the ensemble mean precipitation of the three reanalyses was closer to the observation in both climatology and inter-annual variability than that of any individual reanalysis.

Given the more accurate physical packages and higher resolution, which allows for a better resolved representation of the physical processes in the WRF model compared with the reanalyses model, the former exhibited better performance in terms of climatological mean and inter-annual variability in summer precipitation in both the sensitivity and CTL experiments than those in the original reanalyses. This added value shows that the WRF model produced the expected small-scale information and therefore had good dynamic downscaling skills on the EASM.

Limited by resources, we carried out our experiments with only one RCM, which was forced by three reanalyses and their ensemble mean for 23 EASM cases. This type of study should be repeated under different circulation regimes with varying LB locations, different dynamic core and physical parameterizations of the WRF model, and even different RCMs driven by more reanalyses before generalizing the findings of this work. However, as long as the moisture flux through the LB has large uncertainty, RCM solutions would have large uncertainties. Our additional studies show that the large uncertainty pertaining to moisture among the three reanalyses existed in a large area around the LB location of our model domain (figure not shown). Thus, changing the LB location, the model setup, or even the RCM would only change our results quantitatively. Further comparison of circulation between model simulation and the corresponding reanalysis forcing showed more favorable results, supporting the advantages of the ensemble approach (figures not shown). The ensemble method in this study is the algebraic average. More reasonable ensemble methods will be considered in future work, especially with regard to the moisture field of the reanalyses, which may further reduce uncertainties.

In the EASM region, the primary LB uncertainties of regional climate modeling are found in the moisture flux over the ocean. Although the ensemble approach to large-scale forcing partly reduces these uncertainties and improves model performance, the application of improved satellite data of three-dimensional moisture in future reanalysis might be an essential step forward.

Acknowledgments Hongwei Yang acknowledges joint support from the 973 Project (2010CB428403), 863 Project (2010AA012301), and LASG State Key Laboratory Special fund. Bin Wang at the University of Hawaii acknowledges support by APEC Climate Center (APCC) and the Korean meteorological Administration Research and Development Program under Grant RACS 2010-2017. The authors would also like to thank two anonymous reviewers of this paper for their useful and insightful comments.

References

Adler RF, Huffman GJ, Bolvin DT et al (2000) Tropical rainfall distributions determined using TRMM combined with other satellite and rain gauge information. J Appl Meteorol 39:2007–2023

Adler RF, Huffman GJ, Chang A et al (2003) The version-2 global precipitation climatology project (GPCP) monthly precipitation analysis (1979-present). J Hydrometeorol 4:1147–1167

Anthes RA, Kuo YH, Baumhefner DP, Errico RM, Bettge TW (1985) Predictability of mesoscale atmospheric motions. Issues in atmospheric and oceanic modeling. Advances in geophysics, vol 28B. Academic Press, pp 159–202

Chen F, Dudhia J (2001) Coupling an advanced land surface-hydrology model with the Penn State-NCAR MM5 modeling system. Part I: model implementation and sensitivity. Mon Weather Rev 129:569–585

Chen S-H, Sun W-Y (2002) A one-dimensional time dependent cloud model. J Meteorol Soc Jpn 80:99–118

Christensen JH, Machenhauer B, Jones RG, Schar C, Ruti PM, Castro M, Visconti G (1997) Validation of present-day regional climate simulations over Europe: LAM simulations with observed boundary conditions. Climate Dyn 13:489–506

Christensen OB, Christensen JH, Machenhauer B, Botzet M (1998) Very-high-resolution regional climate simulations over Scandinavia present climate. J Clim 11:3204–3229

Denis B, Laprise R, Caya D, Cote J (2002) Downscaling ability of one-way nested regional climate models: the big-brother experiment. Climate Dyn 18:627–646

Diaconescu EP, Laprise R, Sushama L (2007) The impact of lateral boundary data errors on the simulated climate of a nested regional climate model. Climate Dyn 28:333–350

Ding Y, Sikka DR (2006) Synoptic systems and weather. In: Wang B (ed) The asian monsoon. Springer, Berlin, pp 131–202

Douville H, Chauvin F, Broqua AH (2001) Influence of soil moisture on the Asian and African monsoons. Part I: mean monsoon and daily precipitation. J Clim 14:2381–2403

Dudhia J (1989) Numerical study of convection observed during the winter monsoon experiment using a mesoscale two-dimensional model. J Atmos Sci 46:3077–3107

Fu C-B, Wang S-Y et al (2005) Regional climate model intercomparison project for Asia. Bull Am Meteorol Soc 86:257–266

Giorgi F, Bi X (2000) A study of internal variability of a regional climate model. J Geophys Res 105:29503–29521

Giorgi F, Mearns LO (1999) Introduction to special section: regional climate modeling revisited. J Geophys Res 104:6335–6352

Gustafsson N (2002) Sensitivity of limited area model data assimilation to lateral boundary condition fields. Tellus A 42:109–115

Jacob D, Podzun R (1997) Sensitivity studies with the regional climate model REMO. Meteorol Atmos Phys 63:119–129

Janjic ZI (2000) Comments on ''development and evaluation of a convection scheme for use in climate models''. J Atmos Sci 57:3686

Kanamitsu M, Ebisuzaki W, Woollen J, Yang S-K, Hnilo JJ, Fiorino M, Potter GL (2002) NCEP-DOE AMIP-II reanalysis (R-2). Bull Am Meteorol Soc 83:1631–1643

Krishnamurti TN, Kishtawal CM, LaRow TE, Bachiochi DR, Zhang Z, Williford CE, Gadgil S, Surendran S (1999) Improved weather and seasonal climate forecasts from multi-model superensemble. Science 285:1548–1550

Leung LR, Ghan SJ (1999) Pacific Northwest climate sensitivity simulated by a regional climate model driven by a GCM. Part I: control simulations. J Clim 12:2010–2030

Liang X-Z, Kunkel KE, Samel AN (2001) Development of a regional climate model for US midwest applications. Part I—sensitivity to buffer zone treatment. J Clim 14:4363–4378

Lin Y-L, Farley RD, Orville HD (1983) Bulk parameterization of the snow field in a cloud model. J Clim Appl Meteorol 22:1065–1092

Miyakoda K, Rosati A (1977) One way nested grid models: the interface conditions and the numerical accuracy. Mon Weather Rev 105:1092–1107

Mlawer EJ, Taubman SJ, Brown PD et al (1997) Radiative transfer for inhomogeneous atmosphere: RRTM, a validated correlated-k model for the longwave. J Geophys Res 102:16663–16682

Mohanty UC, Paliwal RK et al (1990) Evaluation of a limited area model for short range prediction over Indian region: sensitivity studies. Mausam 41:251–256

Noh Y, Cheon WG, Hong SY, Raasch S (2003) Improvement of the K-profile model for the planetary boundary layer based on large eddy simulation data. Bound Layer Meteor 107:401–427

Onogi K, Tsutsui J, Koide H et al (2007) The JRA-25 reanalysis. J Meteorol Soc Jpn 85:369–432

Paegle J, Yang Q, Wang M (1997) Predictability in limited area and global models. Meteorol Atmos Phys 63:53–69

Palmer TN, Brankovic C, Richardson DS (2000) A probability and decision-model analysis of PROBOST seasonal multi-model ensemble integrations. Q J R Meteorol Soc 126:2013–2034

Pan Z, Christensen JH, Arritt RW, Gutowski WJ Jr, Takle ES, Otieno F (2001) Evaluation of uncertainties in regional climate change simulations. J Geophys Res 106:17735–17751

Qian Y-F, Liu H-Q (2001) On nesting area selection of regional climate models coupled to a global climate model (in Chinese). Chin J Atmos Sci 25:492–502

Shukla J, Anderson J, Baumhefner D et al (2000) Dynamical seasonal prediction. Bull Am Meteorol Soc 81:2593–2606

Skamarock WC, Klemp JB, Dudhia J et al (2005) A description of the advanced research WRF version 2. NCAR tech notes-468 + STR

Takle ES, Gutowski WJ Jr, Arritt RW et al (1999) Project to intercompare regional climate simulations (PIRCS): description and initial results. J Geophys Res 104:19443–19461

Uppala SM, Kallberg PW, Simmons AJ et al (2005) The ERA-40 re-analysis. Q J Roy Meteorol Soc 131:2961–3012

Vukicevic T, Errico RM (1990) The influence of artificial and physical factors upon predictability estimates using a complex limited-area model. Mon Weather Rev 118:1460–1482

Wang B, Yang H-W (2008) Hydrological issues in lateral boundary conditions for regional climate modeling: simulation of east asian summer monsoon in 1998. Clim Dyn 31:477–490

Wang Y, Sen OL, Wang B (2003) A highly resolved regional climate model (IPRC-RegCM) and its simulation of the 1998 severe precipitation event over China. Part I: model description and verification of simulation. J Clim 16:1721–1738

Wang B, Kang I-S, Lee J-Y (2004) Ensemble simulations of Asian–Australian monsoon variability by 11 AGCMs. J Clim 17:803–818

Wu W, Lynch AH, Rivers A (2005) Estimating the uncertainty in a regional climate model related to initial and lateral boundary conditions. J Clim 18:917–933

Xue Y, Vasic R, Janjic Z, Mesinger F, Mitchell KE (2007) Assessment of dynamic downscaling of the continental U.S. Regional climate using the eta/ssib regional climate model. J Clim 20:4172–4193

Yatagai A, Arakawa O, Kamiguchi K, Kawamoto H, Nodzu MI, Hamada A (2009) A 44-year daily gridded precipitation dataset for Asia based on a dense network of rain gauges. SOLA 5:137–140. doi:10.2151/sola.2009-035

Zhou T-J, Yu R-C (2005) Atmospheric water vapor transport associated with typical anomalous summer rainfall patterns in China. J Geophys Res 110:D08104. doi:10.1029/2004JD005413